




RESEARCH ARTICLE OPEN ACCESS

Comparative Physiology and Morphology of BLA-Projecting NBM/SI Cholinergic Neurons in Mouse and Macaque

Feng Luo¹  | Li Jiang²  | Niraj S. Desai¹ | Li Bai¹ | Gabrielle V. Watkins¹ | Mark A. G. Eldridge³ | Anya S. Plotnikova³  | Arya Mohanty³ | Alex C. Cummins³ | Bruno B. Averbeck³ | David A. Talmage² | Lorna W. Role¹

¹Section on Circuits, Synapses, and Molecular Signaling, National Institute of Neurological Disorders and Stroke, National Institutes of Health, Bethesda, Maryland, USA | ²Section on Genetics of Neuronal Signaling, National Institute of Neurological Disorders and Stroke, National Institutes of Health, Bethesda, Maryland, USA | ³Laboratory of Neuropsychology, National Institute of Mental Health, National Institutes of Health, Bethesda, Maryland, USA

Correspondence: Lorna W. Role (lorna.role@nih.gov) | Feng Luo (feng.luo@nih.gov)

Received: 13 August 2024 | **Revised:** 20 October 2024 | **Accepted:** 6 November 2024

Funding: This study was supported by NINDS Intramural Research Program and NIMH Intramural Research Program (ZIA MH002928).

Keywords: basal forebrain | cholinergic | donkey anti-goat Alexa-Fluor 488 | morphoelectric physiology | mouse | nonhuman primate

ABSTRACT

Cholinergic projection neurons of the nucleus basalis and substantia innominata (NBM/SI) densely innervate the basolateral amygdala (BLA) and have been shown to contribute to the encoding of fundamental and life-threatening experiences. Given the vital importance of these circuits in the acquisition and retention of memories that are essential for survival in a changing environment, it is not surprising that the basic anatomical organization of the NBM/SI is well conserved across animal classes as diverse as teleost and mammal. What is not known is the extent to which the physiology and morphology of NBM/SI neurons have also been conserved. To address this issue, we made patch-clamp recordings from NBM/SI neurons in ex vivo slices of two widely divergent mammalian species, mouse and rhesus macaque, focusing our efforts on cholinergic neurons that project to the BLA. We then reconstructed most of these recorded neurons post hoc to characterize neuronal morphology. We found that rhesus macaque BLA-projecting cholinergic neurons were both more intrinsically excitable and less morphologically compact than their mouse homologs. Combining measurements of 18 physiological features and 13 morphological features, we illustrate the extent of the separation. Although macaque and mouse neurons both exhibited considerable within-group diversity and overlapped with each other on multiple individual metrics, a combined morphoelectric analysis demonstrates that they form two distinct neuronal classes. Given the shared purpose of the circuits in which these neurons participate, this finding raises questions about (and offers constraints on) how these distinct classes result in similar behavior.

1 | Introduction

The basal forebrain cholinergic system is among the most antique parts of the brain, being present in vertebrates as evolutionarily distant as teleosts and primates (Semba 2004). Among mammals, its organization follows a similar anatomical plan across the

rostral–caudal axis that includes the ventral pallidum, medial septum, diagonal band, substantia innominata (SI), and nucleus basalis of Meynert (NBM) (Mesulam, Mufson, Wainer, et al. 1983; Woolf 1991). These nuclei send long-range projections to the cortex, hippocampus, and amygdala and are thought to subserve similar fundamental functions across species: participating in

Feng Luo and Li Jiang are co-first authors.

This is an open access article under the terms of the [Creative Commons Attribution-NonCommercial](https://creativecommons.org/licenses/by-nc/4.0/) License, which permits use, distribution and reproduction in any medium, provided the original work is properly cited and is not used for commercial purposes.

Published 2024. This article is a U.S. Government work and is in the public domain in the USA. The *Journal of Comparative Neurology* published by Wiley Periodicals LLC.

attention and sensory perception, avoidance of aversive or life-threatening situations, and reinforcement of appetitive behaviors. Overall, the cholinergic system for many species is implicated in embedding important experiences in memory (Picciotto, Higley, and Mineur 2012; Ballinger et al. 2016; Knox and Keller 2016; Ananth et al. 2023).

Although the similarities across evolution are striking, there are also notable differences in the structure and composition of the basal forebrain in distinct species. For example, the volume of the nucleus basalis is an order of magnitude larger in nonhuman primates than it is in rodents (Semba 2004), and cholinergic neurons have been estimated to account for as much as 50%–90% of the NBM neurons in primates (Mesulam, Mufson, Levey, et al. 1983; Mesulam and Geula 1988; Bañuelos et al. 2023) but only 5%–20% in rodents (Gritti et al. 2006; Zaborszky, van den Pol, and Gyengesi 2012). This mix of similarities and differences is both perplexing and intriguing. It raises questions both about how different species produce equivalent behaviors and about how their responses might differ.

These questions are especially important with regard to the cholinergic neurons of the NBM/SI that send long-range projections to the basolateral amygdala (BLA). These neurons are part of the survival circuits in the brain that are conserved across mammalian species (LeDoux 2012, 2022; McGaugh 2018; Diehl, Bravo-Rivera, and Quirk 2019). NBM/SI cholinergic neurons send a particularly dense innervation to BLA, and the resulting circuit is engaged in both appetitive (Tye 2018; Crouse et al. 2020) and aversive (Jiang et al. 2016; Rajebhosale et al. 2024) memory encoding. Cued appetitive or aversive stimuli excite NBM/SI cholinergic neurons and lead to increased release of acetylcholine in the BLA (Crouse et al. 2020; Rajebhosale et al. 2024). Acquisition of fear-associated and reward-associated memories is enhanced through increased BLA principal neuron activity, mediated at least in part by cholinergic signaling. Optogenetic stimulation of cholinergic terminals in the BLA reinforces cue–reward learning (Crouse et al. 2020) and extends the durability of fear memory against extinction in mice (Jiang et al. 2016). Likewise, in both rodents and primates, lesions of basal forebrain cholinergic projection neurons, or chemogenetic and/or pharmacological interference with cholinergic signaling, disrupt multiple types of memory acquisition and retention in these species (Ridley et al. 1999; Turchi, Saunders, and Mishkin 2005; Easton et al. 2011; Melamed et al. 2017; Rajebhosale et al. 2024).

In this study, we approach the questions using a bottom-up approach: we characterize the building blocks of cholinergic circuits—namely, the intrinsic electrical properties and morphology of individual cholinergic neurons—with the idea that this will enhance our understanding of circuit computations as a whole. We identified BLA-projecting neurons in NBM/SI in two very different mammalian species, mouse and monkey (rhesus macaque), by retrograde transport of fluorescently labeled microbeads. We determined their cholinergic phenotype by immunohistochemical labeling (monkey) and/or genetic expression of a choline acetyltransferase (ChAT) transgene (mouse) and characterized their intrinsic electrical properties using whole-cell patch-clamp recordings. We reconstructed these physiologically characterized neurons using neurobiotin processing to trace the shapes of their proximal neuritic arbors. We then used

the resulting physiological and morphological measurements, together with standard techniques for dimensionality reduction, to define quantitatively how mouse and monkey neurons in this well-defined set are similar and how they are different at the cellular level.

2 | Materials and Methods

All animal use was conducted under an animal study protocol approved by the NINDS or NIMH Animal Care and Use Committees (ACUC) and conformed to the Institute of Medicine Guide for the Care and Use of Laboratory Animals.

2.1 | Mouse Surgery and Tissue Preparation

Twenty-seven ChAT-tau-GFP mice (Grybko et al. 2011) were used in this study (18 males and nine females, 1.5–3.5 months; Table 1). For microbead injections, mice were anesthetized with isoflurane and positioned in a stereotaxic apparatus (David Kopf Instruments). Eye ointment was applied to prevent the cornea from drying out, and Meloxicam SR (2 mg/mL) was injected subcutaneously to alleviate pain. Using aseptic techniques, a cut along the anterior–posterior axis was made to expose the skull. After craniotomy holes were drilled, a 26-gauge microsyringe (Hamilton) was used to deliver microbeads (FluoSpheres Carboxylate-Modified Microspheres, red F8793; Invitrogen; 200–300 nL) into the BLA (anterior/posterior -1.1 mm from bregma; medial/lateral ± 3.25 mm from bregma; dorsal/ventral -4.15 mm from dura) bilaterally. After injections, the scalp was repositioned using Vetbond (3 M) tissue adhesive, and lidocaine cream was applied topically. Animals were returned to the home cage with a heating pad for recovery.

Five to seven days after surgery, animals were anesthetized with ketamine/xylazine (100 and 10 mg/kg, respectively, delivered i.p.) and transcardially perfused with an ice-cold cutting solution (in mM: 230 sucrose, 2.5 KCl, 10 MgSO₄, 0.5 CaCl₂, 1.25 NaH₂PO₄, 26 NaHCO₃, 10 glucose, and 1.5 sodium pyruvate, pH 7.4, osmolarity 300–310 mOsm) oxygenated with carbogen (95% O₂/5% CO₂). After decapitation, the brain was quickly removed from the skull and immersed for several minutes in an ice-cold oxygenated cutting solution.

Coronal brain slices (250 or 300 μ m) were prepared with a Leica VT1200S vibratome and then transferred to a holding chamber containing artificial cerebrospinal fluid (aCSF) solution (in mM: 126 NaCl, 2.5 KCl, 1.25 NaH₂PO₄, 26 NaHCO₃, 2 CaCl₂, 2 MgCl₂, and 10 glucose, pH 7.4, osmolarity 300–310 mOsm) oxygenated with carbogen. Slices were equilibrated at room temperature (RT) for at least 1 h prior to transfer to a recording chamber perfused with oxygenated aCSF at $31 \pm 0.5^\circ\text{C}$.

2.2 | Monkey Craniotomy and Injection

From 13 total monkeys (*Macaca mulatta*), data on BLA-projecting cholinergic neurons were obtained from nine adults, including seven males (9.8 ± 2.0 years old; ranging from 7.2 to 12.8 years) and two females (6.9 and 16.9 years old; see Table 1 for demographic details and data summary).

TABLE 1 | Summary of electrophysiological data collected from ChAT-tau-GFP mouse and macaque with BLA microbeads injection.

Species	N	Sex	Age	BLA-projecting cholinergic, <i>n</i>	BLA-projecting noncholinergic, <i>n</i>
Mouse	27	18 M; 9 F	5–14 weeks (median 7 weeks)	48	46
Macaque	9	7 M; 2 F	7–17 years (median 10 years)	46	11

Surgeries were carried out in a veterinary operating facility using an aseptic technique. Structural MRIs were used to guide the brain injections (Saunders, Aigner, and Frank 1990). Animals were sedated with ketamine hydrochloride (10 mg/kg), and anesthesia was maintained with isoflurane. Body temperature, heart rate, blood pressure, SpO₂, and expired CO₂ were monitored throughout. Stereotaxic injection coordinates were derived from preoperative structural MRIs (Saunders, Aigner, and Frank 1990; Walbridge et al. 2006). The procedure has been described in detail in previous studies (Fredericks et al. 2020). Microbeads (FluoSpheres Carboxylate-Modified Microspheres, blue F8781 or red F8793; Invitrogen) were sterile filtered (0.45- μ m filter unit; Merck Millipore) and injected in a volume of 20 μ L per site, at 1.0 μ L/min. Three injection sites were placed 2–2.5 mm apart in the dorsoventral plane at each of two anterior–posterior sites 1.5–2.0 mm apart, for a total injection volume of 120 μ L across six sites. In a subset of experiments, AAV.PHP.Eb S9E27::dTom NLS-dTom developed by Dr. Fishell and colleagues (Furlanis et al. 2024) was also used. Accordingly, in some animals, two additional injection sites above anterior NBM/SI were placed 4.0–5.0 mm apart in the mediolateral plane for a volume of 10 μ L per site, at 1.0 μ L/min. However, in all cases, the identification of neurons as cholinergic in monkey was based solely on post hoc staining with ChAT antibody.

2.3 | Monkey Tissue Harvest

On the morning of tissue harvest, each animal was sedated with ketamine hydrochloride (10 mg/kg i.m.) and perfused (70–80 mL/min) with ice-cold slicing buffer (in mM: 90 sucrose, 80 NaCl, 3.5 KCl, 24 NaHCO₃, 1.25 NaH₂PO₄, 4.5 MgCl₂, 0.5 CaCl₂, and 10 glucose, pH 7.4, osmolarity 290–300 mOsm) oxygenated with carbogen, until the lungs were white and no blood came out of the right atrium. The brain was rapidly removed (~5 min) from the skull and submerged in ice-cold carbogen-bubbled aCSF. The brain was separated into two hemispheres and then blocked in the coronal plane at two levels. The first cut was through the most rostral part of the temporal lobe, and the second cut was performed about 13 mm caudal to the first cut at the level of the rostral hippocampus. The isolated tissue was blocked to ~10-mm wide \times 10-mm high \times 6-mm thick to contain only the striatum, the basal forebrain, and the BLA. The tissue block was placed in an ice-cold oxygenated perfusion solution and transported to the electrophysiological laboratory for slicing. Coronal slices at a thickness of 250–300 μ m were obtained using a Leica VT1200S vibratome in an ice-cold cutting solution optimized for aged tissues (Ting et al. 2018). The solution had an osmolarity of ~300 mOsm, was bubbled continuously with carbogen, and contained (in mM): 92 *N*-methyl-D-glucamine (NMDG), 2.5 KCl, 1.25 NaH₂PO₄, 30 NaHCO₃, 20 HEPES, 25 glucose, 2 thiourea, 5 Na-ascorbate, 3 Na-pyruvate, 0.5 CaCl₂·2H₂O, and 10 MgSO₄·7H₂O (titrated to

pH 7.3–7.4 with concentrated hydrochloric acid). Slices were then transferred to a holding chamber that contained carbogen-bubbled solution (in mM): 92 NaCl, 2.5 KCl, 1.25 NaH₂PO₄, 30 NaHCO₃, 20 HEPES, 25 glucose, 2 thiourea, 5 Na-ascorbate, 3 Na-pyruvate, 2 CaCl₂·2H₂O, and 2 MgSO₄·7H₂O; pH 7.4; osmolarity 300–310 mOsm. Slices were equilibrated at RT for at least 1 h prior to recording.

This procedure differs from that employed in the mouse tissue harvest in that slices were cut in an NMDG-based solution rather than a sucrose-based solution. The reason for employing NMDG was to maximize our chances of getting healthy tissue from aged animals (Ting et al. 2018). It is possible that this difference (sucrose-based vs. NMDG-based) contributed to part of the differences in physiological properties we observed between mouse and macaque. We tended to discount this concern because the monkeys, like the mice, were perfused using a sucrose-based solution, and monkey tissue, like mouse tissue, was dissected in a sucrose-based solution. These first steps are known to be especially important (Ting et al. 2018). Even so, readers should be aware of and should consider this caveat.

2.4 | Electrophysiology

Whole-cell patch-clamp recordings were made from neurons in brain slices containing NBM/SI from either mouse or monkey using identical procedures. Slices were perfused continuously with oxygenated aCSF at a rate of 1–2 mL/min and a temperature of 31.0 \pm 0.5°C. The NBM/SI region was located by using the anterior commissure, internal capsule, optic tract, and/or striatum as landmarks (locations of all recorded neurons were confirmed post hoc by relocalization of neurobiotin-filled cells and assessed for the presence or absence of ChAT immunoreactivity, as delineated below). Neurons were selected for recording based on their location and the presence of microbeads from the previous BLA injection. Labeled neurons were visualized with a high-resolution camera on an upright microscope fitted with differential interference contrast optics and a fluorescence microscopy illumination system (SliceScope Pro 6000; Scientifica). Recordings were made with PatchStar manipulators (Scientifica) using borosilicate glass electrodes (4–6 M Ω) pulled on a laser-based puller (P-2000; Sutter) and filled with intracellular solution containing the following (in mM): 125 K-gluconate, 10 KCl, 1 MgCl₂, 10 HEPES, 4 Mg-ATP, 0.3 Na₂-GTP, 7 phosphocreatine, and 0.2% neurobiotin (pH 7.3 corrected with KOH, osmolarity 290–295 mOsm). All recordings were amplified (10 \times) and low-pass filtered (4 kHz) with Multiclamp 700B amplifiers (Molecular Devices), digitized using either a Digidata 1550b (Molecular Devices) or a National Instruments PCIe-6353 board, and acquired at 10 kHz with either pClamp 11 software (Molecular

Devices) or custom scripts written in MATLAB (The MathWorks). Recordings were analyzed offline using custom MATLAB code (see Section 2.5).

Once a recording was in whole-cell (current-clamp) mode and stabilized following equilibration with the intracellular solution, passive and active membrane properties of the neurons were measured using a family of current steps (500 ms duration, -60 to 200 pA amplitude). For these recordings, the baseline membrane potential was adjusted to -65 mV, and current steps were separated by at least 10 s to allow for recovery. Recordings were accepted for offline analysis only if the access resistance (< 25 M Ω) was stable within $< 20\%$, the offset current in whole-cell configuration remained within 10% of its initial value, and the resting membrane potential was ≤ -40 mV. Liquid junction potentials (-14 mV) were not corrected.

2.5 | Electrophysiology Analysis

Eighteen features were extracted from the responses to current steps using custom code (available at <https://doi.org/10.5281/zenodo.10975327>) written in MATLAB (see Figure S2-1A): (1) resting membrane potential (mV), measured in the absence of a current injection; (2) sag potential (mV), measured in response to a -60 -pA step, equal to the difference between the steady-state potential and the minimum potential; (3) input resistance (M Ω), measured by the response to a -20 -pA step; (4) membrane time constant (τ , ms), measured by the relaxation to a -20 -pA step; (5) rheobase (pA), the minimum current step of 500-ms duration needed to elicit an action potential; (6) spike threshold (mV), measured from the first action potential of the rheobase current step (“first action potential”) and defined as the potential at which dV/dt crosses 10 mV/ms; (7) spike amplitude (mV), measured from the first action potential and defined as the difference between the tip of the action potential and the spike threshold; (8) spike width (ms), measured from the first action potential and defined as the width at half maximum (halfway between threshold and tip); (9) spike latency (ms), measured at rheobase current and defined as the time difference between the start of the step and the threshold crossing of the first spike; (10) upstroke (mV/ms), the maximum value of dV/dt on the upstroke of the first action potential; (11) downstroke (mV/ms), the minimum value of dV/dt on the downstroke of the first action potential; (12) afterhyperpolarization potential (AHP) amplitude (mV), measured after the first action potential and defined as the difference between threshold and the minimum potential 100 ms later; (13) AHP latency (ms), the time after spike threshold is crossed by the first action potential and the AHP minimum; (14) AHP width (ms), the time difference at half maximum of the first AHP; (15) $f-I$ slope (Hz/pA), the slope of the initial linear section of the $f-I$ curve; (16) max firing rate (Hz), the maximum firing rate produced by a current step between 0 and 200 pA, across the entire 500-ms duration; (17) adaptation index (dimensionless), for the maximal current step, the number of spikes elicited in the second half of the step divided by the number elicited in the first half; and (18) coefficient of variation (CV; dimensionless) of interspike intervals, measured from the maximal current step.

2.6 | Immunohistochemistry and Imaging

After patch-clamp recordings, sections were fixed in 4% paraformaldehyde in 0.1 M phosphate-buffered saline (PBS) (pH 7.4) overnight at 4°C and transferred to PBS for storage until processing.

For visualization of the neurobiotin-labeled cells in mouse, free-floating sections were rinsed in PBS (3×10 min) at RT before being incubated in streptavidin dye conjugate (Cy5, 1:1000; Sigma) with 2% Triton X-100 over night at 4°C . The slices were washed in PBS (3×10 min) and mounted for imaging with DAPI fluoromount. In control experiments, we contrasted mouse morphological features obtained with standard fixation protocol against those obtained with Clear, Unobstructed Brain Imaging Cocktails (CUBIC): there were no significant differences in measures of proximal arbor metrics (convex hull, complexity, numbers, lengths, etc.; data not shown). Thus, we grouped data from both the standard fixation protocol and CUBIC for analysis.

CUBIC was used for visualization of the neurobiotin-labeled macaque neurons. Free-floating sections were rinsed in PBS (3×60 min) and incubated in CUBIC solution A (25% *N,N,N',N'*-tetrakis(2-hydroxypropyl)ethylenediamine, 25% urea, 15% Triton-X in Milli-Q water) on a shaker for 1–2 days at RT. The procedures for immunohistochemical detection of ChAT were as follows. After being rinsed in PBS (3×60 min), the sections were blocked in a PBS solution containing 10% normal donkey serum and 2% TritonX-100 for 16–24 h on a shaker at 4°C . The blocking solution was used as the diluent in all subsequent antibody solutions. Brain sections were incubated with a goat polyclonal primary antibody (1:250; AB144P; Millipore Sigma) against ChAT, shaking at 4°C for 6 nights. Following primary antibody incubation, sections were washed in dilution buffer (3×60 min) at RT (20 – 25°C) and incubated in donkey anti-goat Alexa-Fluor 488 (1:1000) and streptavidin dye conjugate (Cy5, 1:1000; Sigma) for 16–24 h at 4°C . Sections were rinsed in PBS (2×60 min) and transferred to CUBIC solution B (50% sucrose, 25% urea, 10% Triethanolamine, 0.1% Triton-X 100 in Milli-Q water) on a shaker overnight at RT. All incubations were conducted in darkness. Sections were mounted on Superfrost Plus glass slides and cover-slipped with CUBIC solution B. Coverslips were then sealed with clear nail polish (Electron Microscopy Sciences) and stored in a slide box at 4°C until imaging within 2–4 h.

Z-stacks of brain slices were imaged on a slide scanner (VS200; Olympus) for cell relocalization, and individual neurobiotin-relocated NBM/SI neurons were imaged on a confocal microscope (LSM800; Zeiss) using a $20\times$ objective. Stacks were collected at a 1- to $2\text{-}\mu\text{m}$ slice interval, stepping through the entire soma and all visible processes of the neuron. All scans containing z-stack images were saved as CZI files (Olympus) for subsequent quantitative analysis.

2.7 | Cell Reconstruction and Morphological Analysis

Confocal images of relocalized cells were imported to Imaris 9 software (Oxford Instruments) for filament tracing. Images were

processed to remove background noise, and automated detection was used for morphological reconstruction of all neurites. The autogenerated filaments were fine-tuned manually to eliminate mis-detected branches and/or to add back undetected branches. Thirteen morphological features were quantified (Figure S2-1C,D) using these reconstructions.

The 13 features were defined as follows. (1) Total process area (μm^2) is the summed surface area of all processes extending from the soma. This measurement excludes the area of the soma itself. (2) Total process length (μm) is the summed length of all processes extending from the soma. (3) Number of primary processes is the number of processes emerging directly from the soma. (4) Total process length normalized is the total process length divided by the number of primary processes. (5) Number of branch points is the total number of branching points in the whole neuritic tree. (6) Branch point normalized is the number of branch points divided by the number of primary processes. (7) Number of first-order processes is the number of branches emerging from a primary process. (8) Number of second-order processes is the number of branches emerging from a first-order process. (9) Root angle (rad) was measured as in Bird and Cuntz (2019) using the TREES Toolbox (www.treestoolbox.org) (Bird and Cuntz 2019). The root angle at a particular point is defined as the angle between the tangent line at that point and a line directly connecting the point to the soma (see Figure S2-1C). We measured the root angles at all points along the whole tree and calculated their average. (10) Centripetal bias (κ , dimensionless) was estimated by fitting the distribution of root angles to the 3D von Mises distribution. The centripetal bias is roughly equivalent to the inverse of the distribution's variance ($1/\sigma^2$). Centripetal bias is a measure of how directly a neuron's dendritic branches point toward the soma. Neurons with strong centripetal bias (e.g., dentate gyrus granule cells) have branches that are disproportionately directed in (roughly) straight lines toward the soma, which tends to minimize synaptic conduction delays. Neurons with weak centripetal bias (e.g., cerebellar Purkinje cells) have more complicated trees, with some branches running parallel to or even away from the soma. This meandering arrangement may impose longer conduction delays on synaptic inputs, but it may also allow neurons to minimize metabolic costs associated with large lengths of dendritic cable, because they can employ convergent branch points (reminiscent of the hubs of air travel) to connect synapses with the soma. Centripetal bias is therefore used to understand the trade-offs neurons make between minimizing conduction delays and minimizing metabolic costs (Bird and Cuntz 2019).

The convex hull is the minimal convex polyhedron that encloses all points of the whole arbor (see Figure S2-1D). Convex Hull XTension (Oxford Instruments) was used to calculate the convex hull for each reconstruction. From this convex hull, three measurements were taken: (11) convex hull area (μm^2), (12) convex hull volume (μm^3), and (13) convex hull sphericity (dimensionless). Sphericity is defined as the ratio of the area if the entire convex hull volume were confined to a sphere and the measured convex hull area. A sphere is the most compact shape possible, and so the ratio will differ from (be smaller than) 1 depending on how nonspherical the convex hull shape is.

In addition to these 13 morphological measurements, which were our principal measures, we also calculated Sholl intersections

in 3D (sphere) data sets with Imaris Filament Sholl Analysis. The script detects the filament starting point and calculates the intersections along the filament segments every 10 μm from the starting point.

2.8 | Statistical Analysis

Statistical analyses were performed using MATLAB and its Statistics and Machine Learning Toolbox. Averages are represented as mean \pm *SD*.

Each of the 18 physiological features extracted from the responses to current steps was compared between groups using a nonparametric Wilcoxon rank-sum test. A *p*-value less than 0.05 was taken to indicate significance. The same applied to the 13 morphological features.

To visualize group differences from many distinct features in two dimensions, we used the Uniform Manifold Approximation and Projection (UMAP) algorithm (McInnes et al. 2018). For all physiological recordings and/or morphological reconstructions used in each comparison, measured features were rendered dimensionless and of unit variance by *z*-score normalization across the data set. A principal component analysis (PCA) was run to reduce dimensionality and minimize the effects of noise. Principal components that accounted for > 1% of variance were retained. These were mapped onto two UMAP dimensions using a MATLAB implementation of the UMAP algorithm (see MATLAB Central File Exchange at <https://www.mathworks.com/matlabcentral/fileexchange/71902> by Meehan and others). Linear discriminant analysis (LDA) was performed using the MATLAB function *Fitcdiscr*.

3 | Results

3.1 | Electrophysiology in the Mouse: Cholinergic Versus Noncholinergic BLA-Projecting NBM/SI Neurons

We first examined the electrophysiological properties of BLA-projecting NBM/SI neurons using whole-cell patch-clamp recordings in mouse brain slices (see complete workflow; Figure 1). One week before each recording session, red fluorospheres ("microbeads") were injected bilaterally into the BLA of ChAT-tau-GFP mice (Figure 1A). The beads were taken up by axonal terminals in the BLA and transported retrogradely to projection areas, including NBM/SI. This allowed us to identify BLA-projecting NBM/SI neurons in brain slices by checking for red fluorescence (Figure 1B, "Beads"). ChAT-tau-GFP mice express the tau-GFP fusion protein under the control of a ChAT promoter such that green fluorescence is expressed throughout the cholinergic neurons and their arbors (Figure 1B, "GFP"). Therefore, we were able to identify both BLA-projecting cholinergic (red + green) and BLA-projecting noncholinergic (red only) neurons in our recordings. We verified our neuron identification in two ways. First, immediately after slice preparation, before whole-cell patch-clamp recordings, we checked that the bead injection site was in BLA (Figure 1B, micrograph at left; Figure S1-1). Second, slices were fixed and processed for confocal imaging after the

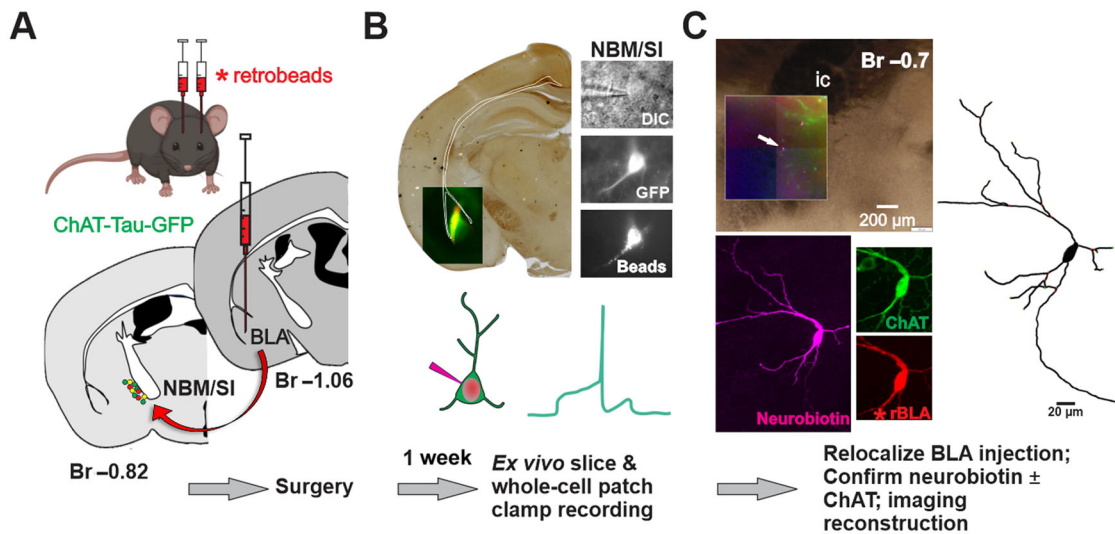


FIGURE 1 | Workflow for morphoelectric profiling of NBM/SI BLA-projecting cholinergic and noncholinergic neurons in mouse. See Figures S1-1 and S1-2. **A.** Surgical back labeling: Schematic for stereotactic injection of fluorescently tagged microbeads (“retrobeads”) bilaterally into BLA of ChAT-tau-GFP mice. The red-labeled beads were taken up by axonal terminals and transported retrogradely to cell bodies in the NBM/SI. This resulted in yellow neurons (both cholinergic and BLA-projecting), red neurons (BLA-projecting but noncholinergic), and green neurons (cholinergic but non-BLA-projecting). **B.** Live imaging and recording: Roughly 1 week after the bead injection, mice were prepared for ex vivo slice recording. (Top left) Photomicrograph of sample injection site of red beads into the BLA of a ChAT-tau-GFP mouse. Yellow and green signals in BLA derive from the extensive (green fluorescent) cholinergic terminal fields within this area. (Top right) Photomicrographs taken during the recording session in the region of the NBM/SI. Cells were first identified in DIC (top). ChAT-tau-GFP labeling was readily detected in live imaging of NBM/SI cholinergic neurons. BLA-projecting neurons were also easily detectable in live imaging due to red beads from the BLA injection. Neurons labeled with both GFP (ChAT) and red beads were classified as both BLA-projecting and cholinergic. Red beads without an overlapping green label were identified as BLA-projecting but noncholinergic. All neurons were filled with neurobiotin during electrophysiological recording. **C.** Relocalization: Neurons were relocalized based on coordinates and neurobiotin processing with streptavidin. Relocalized neurons were further processed for ChAT staining and microbeads labeling to confirm prior identification.

recording session. Neurons that had been filled with neurobiotin during the whole-cell recordings could be relocalized by staining the neurobiotin with streptavidin (Figure 1C). Not only did this postrecording procedure allow us to double-check for red (bead-labeled) and green (ChAT⁺) fluorescence, but it also allowed us to make morphological reconstructions of physiologically characterized neurons (as described in the next section).

In total, 48 BLA-projecting NBM/SI cholinergic neurons and 46 BLA-projecting noncholinergic neurons were recorded in 56 brain slices from 27 animals (18 males, nine females; Table 1). Cell relocalization indicated that 89% of the recorded neurons were located between bregma -0.46 and -0.94 mm, covering the full rostral-caudal axis of the NBM/SI (Figure S1-2).

Intrinsic electrophysiological properties were characterized by injecting a family of current steps (500-ms duration) with amplitudes between -60 and $+200$ pA. To standardize measurements, recordings were made from a baseline potential of -65 mV, maintained by a small offset current (offset currents had to be less than -100 pA to pass quality control). Sample traces at rheobase (Figure 2A, left) and at maximum current injection (Figure 2A, right) are shown for two typical BLA-projecting NBM/SI neurons (cholinergic: teal; noncholinergic: gray). The responses to the current steps were used to extract 18 electrophysiological features representing both subthreshold (e.g., resting input resistance and sag potential) and suprathreshold intrinsic properties (e.g., spike threshold and

subsequent active currents; Figure S2-1A). Average phase plots constructed from the rheobase current step were also used to illustrate differences in action potential kinetics (Figures 2B and S2-1B). The results are shown in Figures 2 and S2-2.

Cholinergic and noncholinergic BLA-projecting neurons within the region of the NBM/SI differed electrophysiologically in all but three features (Figures 2D and S2-2). Overall, noncholinergic neurons were much more excitable than cholinergic ones, with a maximum firing rate almost six times larger (cholinergic 7.3 ± 4.3 Hz, noncholinergic 39.0 ± 24.9 Hz, $p < 0.0001$). This difference was driven both by changes in spike generation (spike threshold: cholinergic -33 ± 4.6 mV, noncholinergic -37.1 ± 6.3 mV, $p < 0.001$; rheobase current: cholinergic 64.3 ± 41.2 pA, noncholinergic 42.2 ± 33.2 pA, $p < 0.001$) and by changes in afterhyperpolarization (AHP amplitude: cholinergic 28.9 ± 8.3 , noncholinergic 12.4 ± 6.1 mV, $p < 0.0001$; AHP width: cholinergic 177.9 ± 89.3 ms, noncholinergic 85.0 ± 118.6 ms, $p < 0.0001$) with concomitant effects on spike frequency adaptation (adaptation index: cholinergic 0.83 ± 0.56 , noncholinergic 0.64 ± 0.29 , $p < 0.05$). Passive electrophysiological properties, such as resting membrane potential (cholinergic -54.4 ± 8.4 mV, noncholinergic -58.7 ± 8.2 mV, $p < 0.05$) and membrane time constant tau (cholinergic 34.6 ± 14.3 , noncholinergic 22.3 ± 9.8 ms, $p < 0.0001$), also exhibited significant differences.

Although there was considerable variability in each feature assayed within the cholinergic and noncholinergic groups and

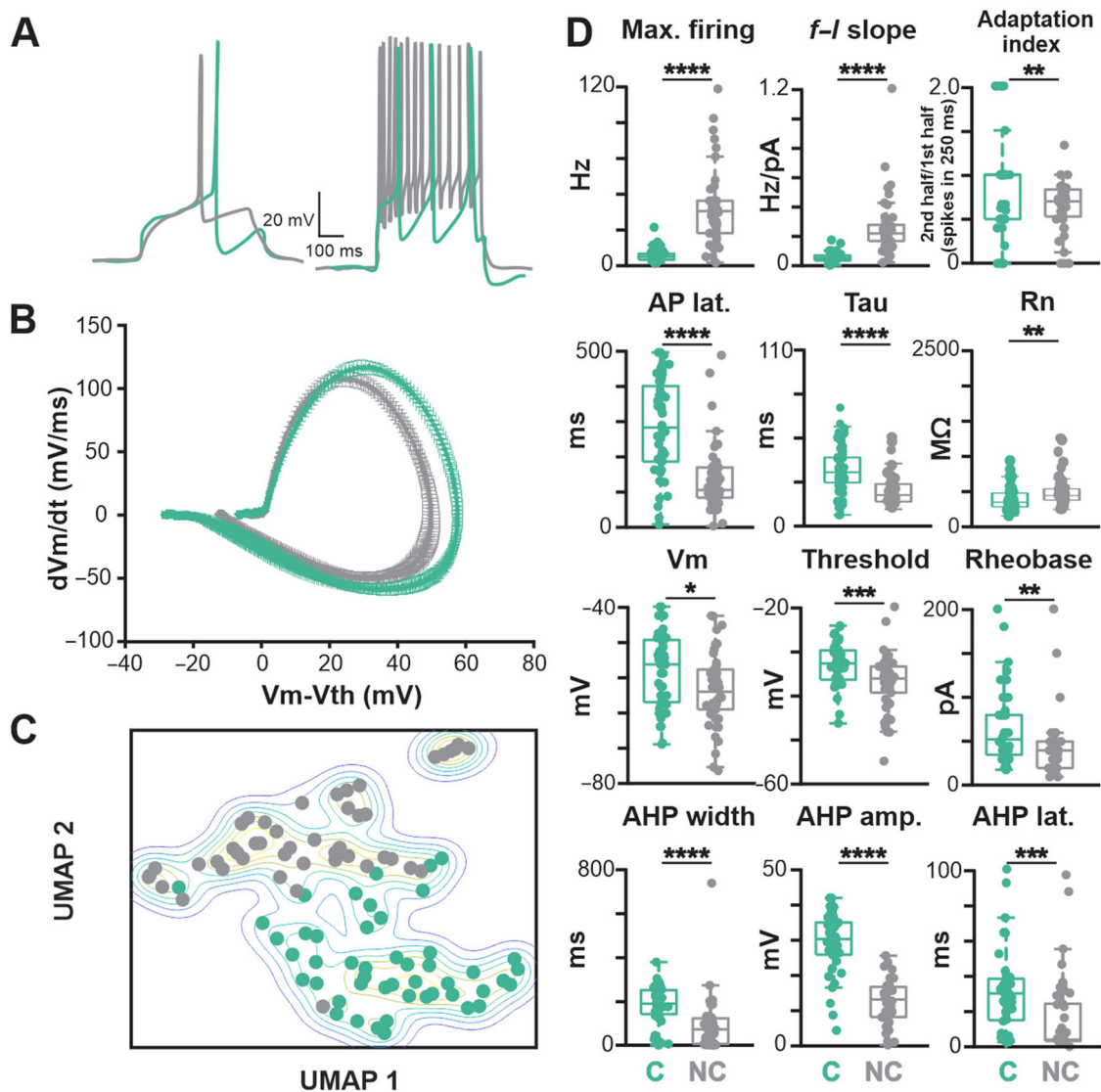


FIGURE 2 | Electrophysiological features consistent with the lower excitability of mouse cholinergic BLA-projecting NBM/SI neurons compared with neighboring noncholinergic BLA-projecting NBM/SI neurons. See Figures S2-1 and S2-2. A. Sample traces at rheobase (left) and at maximum current injection (right; 200 pA) are shown for typical BLA-projecting NBM/SI neurons (cholinergic: teal; noncholinergic: gray). B. Average phase plots illustrate differences in action potential kinetics comparing BLA-projecting NBM/SI neurons (cholinergic: teal; noncholinergic: gray). C. Nondimensional (UMAP) plot of all 18 electrophysiological features comparing BLA-projecting NBM/SI neurons (cholinergic: teal; noncholinergic: gray). D. Population scatter plus box plots of all data for the 12 features that most strongly distinguish BLA-projecting NBM/SI cholinergic neurons ($n = 48$) from their neighboring BLA-projecting, noncholinergic neurons ($n = 46$; cholinergic: teal; noncholinergic: gray). The p -value symbols used in this and all subsequent figures are as follows: * $p \leq 0.05$; ** $p \leq 0.01$; *** $p \leq 0.001$; **** $p \leq 0.0001$. C, cholinergic ($n = 48$); NC, noncholinergic ($n = 46$).

considerable overlap between them in many features, the differences taken as a whole were so strong that unbiased, PCAs clearly separated cholinergic from noncholinergic BLA-projecting NBM/SI neurons. We demonstrated this by reducing dimensionality by running the 18 physiological features through a PCA, discarding PCA components that accounted for $< 1\%$ of the variance. We displayed the remaining components in two dimensions using the UMAP algorithm (McInnes et al. 2018). The resulting UMAP plot (Figure 2C) from this unsupervised classification shows almost complete separation between the BLA-projecting cholinergic and noncholinergic neurons within the NBM/SI; only two neurons fall on the “wrong” side of the boundary.

3.2 | Morphology in the Mouse: Cholinergic Versus Noncholinergic BLA-Projecting NBM/SI Neurons

BLA-projecting neurons were filled with neurobiotin during recordings to allow us to reconstruct and quantify the proximal neuritic arbors of recorded neurons. Mouse BLA-projecting NBM/SI neurons, whether cholinergic or noncholinergic, showed considerable morphological diversity in their proximal arbors (Figure 3, cholinergic; Figure S3-1, noncholinergic). Across the rostral–caudal axis, most neurons were multipolar in shape. The proximal arbors of some spanned several hundreds of microns from the soma, while others appeared limited to within



FIGURE 3 | Skeletonized renditions of relocalized BLA-projecting cholinergic neurons within NBM/SI along all bregma in mouse. See Figure S3-1. The proximal 100^+ μm of the processes emanating from cholinergic somata were morphologically diverse and independent of location along bregma. Most neurons were multipolar, although fairly simple in morphology ($n = 31$).

~ 100 μm of the soma boundary. As in our electrophysiological analysis, BLA-projecting neurons were identified by the presence of red microbeads and divided into cholinergic and noncholinergic categories by the presence or absence of ChAT expression (ChAT tau-GFP; Figure 4A,B).

We used a total of 13 measured features to characterize neuritic morphology, including total process length, number of branch points, convex hull area, and convex hull sphericity (Figure S2-1C,D). In contrast to the electrophysiological differences between neighboring cholinergic and noncholinergic BLA-projecting NBM/SI neurons, we found major similarities with respect to proximal neuritic morphology (Figures 4 and S4-1). Three of the 13 features assayed were statistically significantly different (Figure 4D): cholinergic neurons had more branch points (cholinergic 8.1 ± 5.4 , noncholinergic 6.6 ± 5.4 , $p < 0.05$), a smaller total proximal process area (cholinergic $4.6 \pm 2.7 \times 10^3$ μm^2 , noncholinergic $6.6 \pm 3.6 \times 10^3$ μm^2 , $p < 0.05$), and a smaller centripetal bias (cholinergic 12.9 ± 14.9 , noncholinergic 15.2 ± 10.1 , $p < 0.05$).

On a standard Sholl analysis of intersections as a function of distance from the soma, cholinergic and noncholinergic neurons were also not significantly different (Figure S4-1A). Dimensionality reduction via PCA and subsequent display via UMAP likewise indicated that proximal neuritic morphology was

similar between the two types of mouse BLA-projecting neurons (Figure 4C).

We also used LDA on both the electrophysiological features and the morphological features. LDA is a supervised classification scheme that attempts to find linear combinations of features that best separate distinct groups, which are specified beforehand. In this case, the specified groups were BLA-projecting cholinergic neurons and BLA-projecting noncholinergic neurons. Given the clean separation between these groups on the unsupervised electrophysiological UMAP plot (Figure 2C), supervised LDA revealed a clear separation (Figure 5A). The feature with the highest weight in the LDA vector was AHP amplitude (Figure 5B). By contrast, even supervised LDA failed to separate cholinergic and noncholinergic neurons morphologically (Figure 5C,D). Indeed, the distribution was equivalent to the LDA plots that resulted when feature values were randomly shuffled (Figure 5C, inset).

Together, the data from this part of our study indicate that among BLA-projecting NBM/SI neurons, there are strong differences in the electrophysiological characteristics of cholinergic and neighboring noncholinergic neurons, with the latter having multiple features consistent with a higher level of excitability. Interestingly, there is also a disconnect between physiological and morphological properties with only the former distinguishing cholinergic NBM/SI neurons from noncholinergic neighbors.

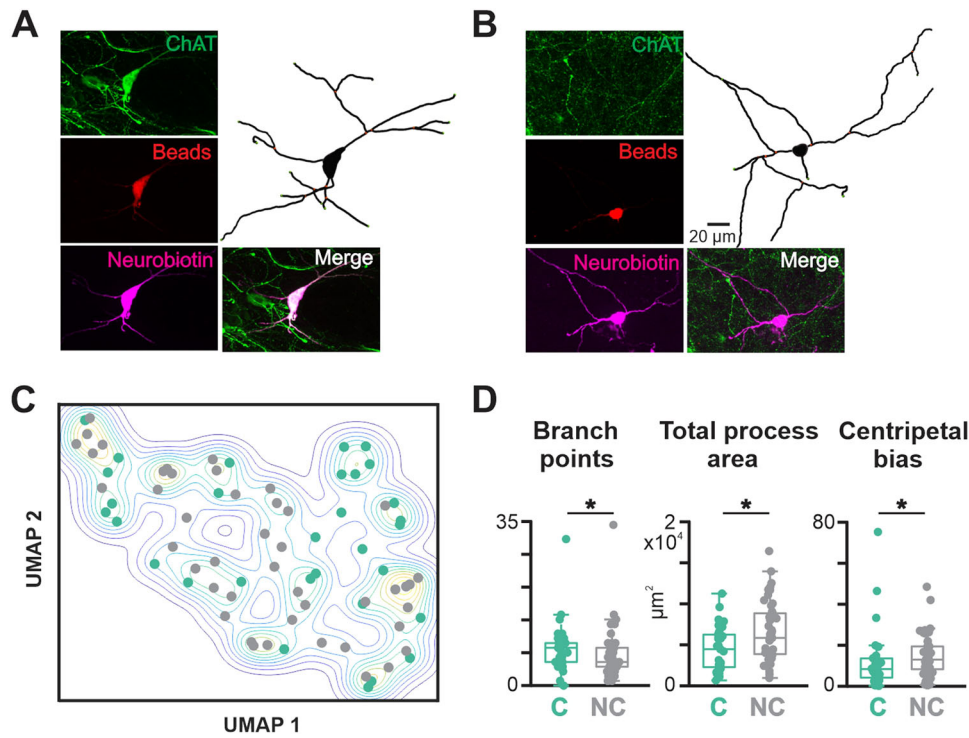


FIGURE 4 | BLA-projecting NBM/SI neurons in mouse, whether cholinergic or noncholinergic, differ in three of the 13 morphological parameters assessed. See Figure S4-1. A. Confocal images of a representative BLA-projecting cholinergic neuron in mouse. B. Confocal images of a representative BLA-projecting noncholinergic neuron in mouse. C. Nondimensional (UMAP) plot of the morphological features of BLA-projecting NBM/SI neurons (cholinergic: teal; noncholinergic: gray). D. Population scatter plus box plots of data for the three morphological features differed significantly between BLA-projecting NBM/SI cholinergic neurons ($n = 31$) and their neighboring BLA-projecting, noncholinergic neurons ($n = 44$; cholinergic: teal; noncholinergic: gray). “C” stands for cholinergic, and “NC” stands for noncholinergic.

3.3 | Electrophysiology of BLA-Projecting NBM/SI Cholinergic Neurons: Mouse Versus Macaque

Previous reports emphasizing how the cholinergic system is conserved between species (Semba 2004) led us to ask which cellular properties of BLA-projecting NBM/SI cholinergic neurons might be shared and which might differ between mouse and macaque. To answer this question, we focused on a definable class of basal forebrain cholinergic neurons, comparing only BLA-projecting NBM/SI cholinergic neurons. We developed a workflow to characterize the electrophysiological and morphological properties of BLA-projecting NBM/SI neurons in the macaque that paralleled our studies in the mouse (Figures 6 and S6-1). With an MRI-guided surgical procedure, we injected fluorescent microbeads into macaque BLA to target the basal forebrain neurons that project to the BLA (see methods for procedures for stereotaxic injection; Figures 6A and S6-1A). After allowing at least 6 weeks for microbeads to move in a retrograde direction to the NBM/SI, the monkeys were euthanized, and brain tissue was removed. The tissue from a given animal was blocked into a small piece containing basal forebrain for slice collection and incubation (Figure S6-1B,C). After verifying the presence of microbeads in BLA (Figures 6C and S6-2), bead-labeled NBM/SI neurons were targeted for whole-cell patch-clamp recording (Figures 6B and S6-1D). These neurons were later relocalized based on coordinates and neurobiotin and then confirmed as positive by ChAT immunolabeling (Figure 6C).

In total, we successfully relocalized 52 BLA-projecting cholinergic neurons and 11 BLA-projecting noncholinergic neurons from nine macaques. The approximate bregma location of all relocalized neurons is shown in Figure S6-3. Most neurons were found at bregma positions between -4.95 and -7.65 mm. This range is comparable to the bregma range we used in mouse (-0.46 to -0.94 mm) based on local anatomical landmarks and covered the major portion of the macaque NBM/SI. In macaque NBM/SI, the density of cholinergic neurons is thought to be much greater than in comparable regions of mouse (Mesulam, Mufson, Levey, et al. 1983). Because of the relatively low number of BLA-projecting noncholinergic neurons in our monkey samples compared with mouse, we focused our analyses on just the cholinergic neurons identified as BLA-projecting when comparing the two species.

Forty-six of the 52 relocalized macaque cholinergic neurons obtained from 38 brain slices passed quality control for inclusion in the study (see Section 2). As in our mouse studies, the properties were characterized using a family of current steps (500 ms duration, -60 to $+200$ pA amplitude) from a baseline potential of -65 mV. Sample traces from representative macaque and mouse neurons are shown in Figure 7A.

We found significant differences between macaque and mouse BLA-projecting cholinergic neurons in intrinsic excitability, with macaque neurons being more excitable. The maximum firing rate was three times larger (macaque 26.3 ± 23.1 Hz, mouse

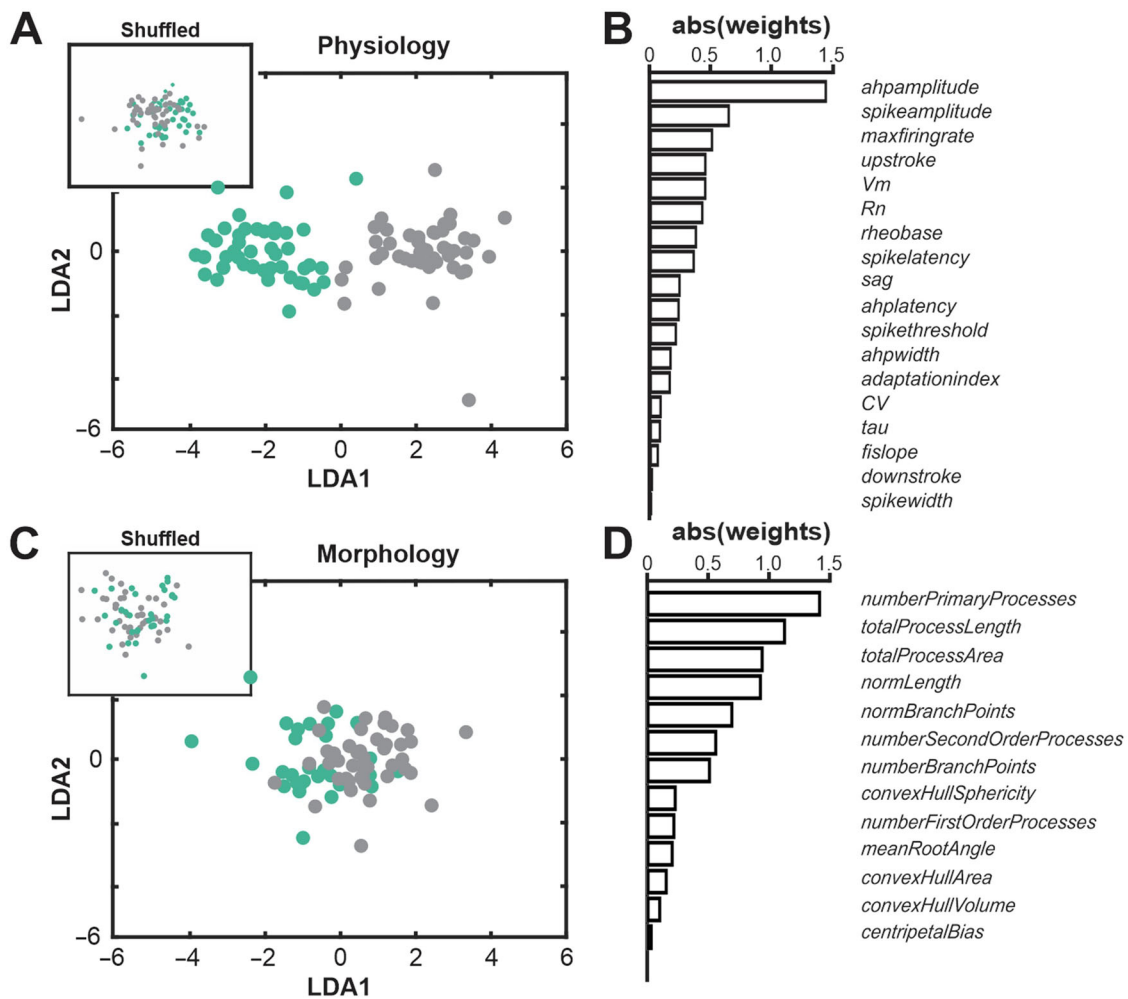


FIGURE 5 | Linear discriminant analysis (LDA) strongly distinguishes cholinergic from noncholinergic BLA-projecting NBM/SI mouse neurons based on electrophysiological, but not on morphological, features. A. LDA was applied to all electrophysiological features for BLA-projecting NBM/SI neurons (cholinergic: teal, $n = 48$; noncholinergic: gray, $n = 46$). There is clear separation in clustering of the two populations from one another but not from the distribution of shuffled data (shown in inset), consistent with the many electrophysiological features that distinguish between BLA-projecting cholinergic versus noncholinergic neurons in mouse. B. Plot of the absolute values of the weighted differences in electrophysiological features between BLA-projecting NBM/SI neurons (cholinergic: teal; noncholinergic: gray). C. LDA was applied to all morphological features for BLA-projecting NBM/SI neurons (cholinergic: teal, $n = 31$; noncholinergic: gray, $n = 44$). The two populations do not separate from one another nor is the distribution of morphological features very different from the shuffled data (shown in inset). D. Plot of the absolute values of the weighted differences in morphological features between BLA-projecting NBM/SI neurons (cholinergic: teal; noncholinergic: gray) of mouse.

7.3 ± 4.3 Hz, $p < 0.0001$), the rheobase current was only a third as large (macaque 23.3 ± 16.5 pA, mouse 64.3 ± 41.2 pA, $p < 0.0001$), and the slope of the f - I curve was twice as large (macaque 0.13 ± 0.10 , mouse 0.06 ± 0.03 , $p < 0.0001$). The higher maximal firing rate of macaque neurons resulted from a combination of changes in spike generation (spike threshold: macaque -39.7 ± 5.9 mV, mouse -33.0 ± 4.6 mV, $p < 0.0001$) and in afterhyperpolarization properties (AHP amplitude: macaque 19.1 ± 8.8 mV, mouse 28.9 ± 8.3 mV, $p < 0.0001$; AHP width: macaque 106.6 ± 71.9 ms, mouse 177.9 ± 89.3 ms, $p < 0.0001$). Macaque neurons also differed from mouse neurons in basic spike shape (spike width: macaque 1.32 ± 0.45 ms, mouse 1.15 ± 0.43 ms, $p < 0.01$), especially evident in the average phase plots (Figures 7B and S7-1B). In all, 15 of the 18 electrophysiological features were insignificantly different between macaque and mouse (Figures 7D and S7-1A,C).

As before, we used dimensionality reduction with PCA to investigate how distinct the two groups were from each other. The resulting 2D UMAP plot is given in Figure 7C. It exhibits a strong separation between groups.

3.4 | Morphology of BLA-Projecting NBM/SI Cholinergic Neurons: Mouse Versus Macaque

Next, we compared the morphological features of the proximal neuritic arbor of BLA-projecting NBM/SI cholinergic neurons in macaque to those in mouse. Reconstructions of all relocated macaque cholinergic neurons are shown in Figure 8, with the neurons arrayed along the rostral-caudal axis. As in the mouse, the proximal arbors of macaque BLA-projecting cholinergic neurons were morphologically diverse, with all neurons appearing to be multipolar and relatively simple.

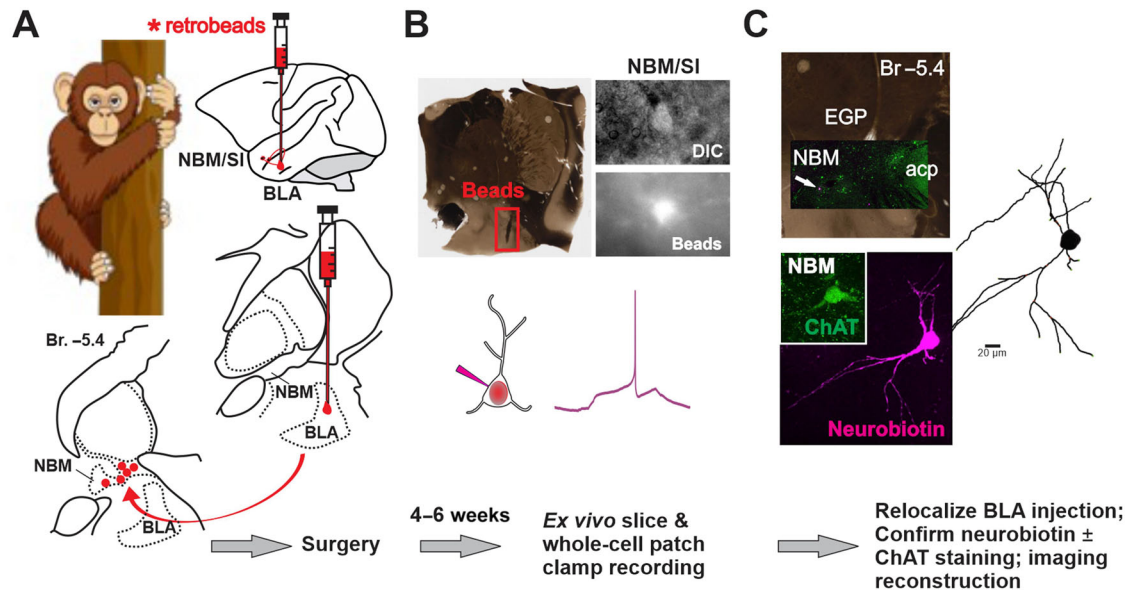


FIGURE 6 | Workflow for morphoelectric profiling of BLA-projecting NBM/SI cholinergic neurons in macaque. See Figures S6-1, S6-2, and S6-3. **A.** Surgical retrograde labeling (top): Schematic for injection of fluorescently tagged microbeads (“retrobeads”) into the BLA of rhesus macaque. Guided by MRI images and stereotaxic coordinates, red microbeads were injected into BLA of rhesus macaque monkeys. These were taken up by axonal terminals and transported retrogradely to the cell bodies of projection neurons in the NBM/SI. **B.** Live imaging and recording: Four to six weeks after microbead injection, sections were prepared for ex vivo slice recording. (Top right) Photomicrographs taken during the recording session in the region of the NBM/SI. Cells were identified in DIC (top) and BLA-projecting neurons detected in live imaging by microbeads from the BLA injection. Bead-positive neurons were filled with neurobiotin during electrophysiological recording. **C.** Relocalization: Neurons were relocated based on coordinates and neurobiotin staining. ChAT labeling was confirmed by immunostaining and high-power images of the cell body, and proximal dendrites were taken for subsequent import into Imaris for morphological parameter assessment.

We measured 13 morphological features from macaque neurons (Figures 9D and S9-1B) and compared these to the same measurements from mouse neurons. Although many morphological features were similar (Figure S9-1A), five of the 13 measured parameters exhibited significant differences. Most notably, those related to convex hull were different (convex hull volume: macaque $2.19 \pm 1.63 \times 10^3 \mu\text{m}^3$, mouse $0.94 \pm 0.77 \times 10^3 \mu\text{m}^3$, $p < 0.0001$; convex hull area: macaque $1.15 \pm 0.59 \times 10^5 \mu\text{m}^2$, mouse $0.83 \pm 0.45 \times 10^5 \mu\text{m}^2$, $p < 0.05$; convex hull sphericity: macaque 0.65 ± 0.08 , mouse 0.51 ± 0.09 , $p < 0.0001$). Two representative images of BLA-projecting NBM/SI cholinergic neurons with fitted convex hulls are shown in Figure 9A,B. In well-characterized neurons, convex hull is used as a representation of the maximal expanse of the dendritic arbor (Bird and Cuntz 2019). The larger convex hull volume and area indicate that macaque neurons occupy more 3D physical space than the comparable mouse neurons (Figures S9-2 and S9-3), whereas the larger sphericity indicates that macaque cholinergic neurons are fuller and mouse neurons are flatter.

Using PCA to reduce dimensionality and UMAP to visualize significant PCA vectors in two dimensions, we obtained the UMAP plot of Figure 9D. There was a tendency for macaque neurons to cluster away from mouse neurons (Figure 9C), but the effect of clustering based on morphology alone was weak—compared, for example, to the electrophysiological UMAP of Figure 7C.

Finally, we combined the electrophysiological and morphological measures for an integrated analysis of morphoelectric features and asked how well this combination distinguished

between BLA-projecting cholinergic neurons from the NBM/SI of macaque and mouse. The results are given in Figure 10. In these analyses, we limited ourselves to samples for which we had electrophysiological recordings that had passed all quality control and that were successfully relocated and confirmed as BLA-projecting and cholinergic (46 macaque neurons and 27 mouse neurons). First, we tried unsupervised classification as before by running numbers through a PCA, retaining PCA vectors that captured at least 1% of the variance, and then visualizing the PCA results in two dimensions using the UMAP method (Figure 10A). Second, we tried supervised classification using LDA (Figure 10B), where macaque and mouse neurons were explicitly categorized. The features with the highest weight in the LDA vector analysis differentiating macaque from mouse were convex hull in morphology and rheobase, AHP width, and maximum firing rate in physiology (Figure 10C).

4 | Discussion

The primary purpose of this study was to assess the similarities and differences between mouse and macaque basal forebrain cholinergic projection neurons. To make the comparison as meaningful as possible, we focused on a subset of neurons located within the NBM/SI that project to the BLA. These neurons have a function in fear learning and memory that is conserved across evolutionary time (Johansen et al. 2011; Dal Monte et al. 2015; Gore et al. 2015; Sah, Sun, and Gooch 2020; Murray and Fellows 2022). We assessed 18 passive and active electrophysiological features and 13 morphological features in each of the recorded

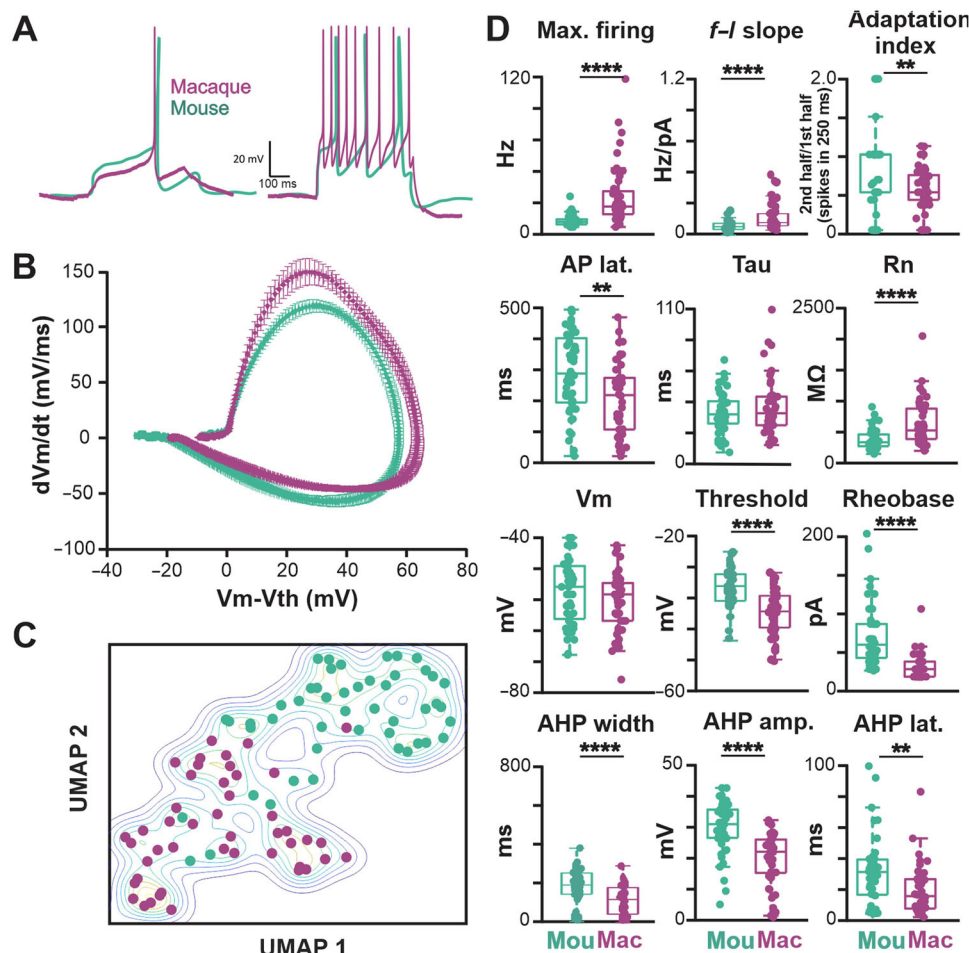


FIGURE 7 | Both passive and active membrane properties of macaque BLA-projecting NBM/SI cholinergic neurons are consistent with higher excitability than those of mouse. See Figure S7-1. A. Sample traces from BLA-projecting cholinergic NBM/SI macaque neurons at rheobase (left) and at maximum current injection (right; 200 pA) are shown (macaque: purple; mouse: teal). Mouse data (from same database of BLA-projecting cholinergic neurons as in Figure 2A) are shown here again for comparison purposes. B. Average phase plots illustrate differences in action potential kinetics between macaque, BLA-projecting NBM/SI cholinergic neurons (purple) and mouse (teal); mouse data are the same as those in Figure 2B, presented here for comparison purpose. C. Nondimensional (UMAP) plot of all 18 electrophysiological features comparing BLA-projecting NBM/SI cholinergic neurons from macaque (purple) with comparable samples from mouse (teal). Mouse data are the same as those in Figure 2C, presented here for ease of comparison. D. Population scatter plus box plots of data for 12 features that distinguish BLA-projecting NBM/SI cholinergic neurons of the rhesus macaque ($n = 46$; purple) from BLA-projecting NBM/SI cholinergic neurons from mouse ($n = 48$; teal). Mouse data are the same as those in Figure 2D presented here for ease of comparison.

neurons. In total, 30 mice were surgically back-labeled with fluorospheres, and 122 BLA-projecting neurons were sampled. For comparison, 13 macaques were examined yielding 83 BLA-projecting neurons. Between 70% and 80% of the back-labeled BLA-projecting neurons (mouse 107; macaque 57) passed initial quality control and were processed for relocation based on neurobiotin filling, with 80%–90% successfully relocated. In total, we obtained complete analyses of 94 BLA-projecting neurons (48 cholinergic and 46 noncholinergic for electrophysiology; 31 cholinergic and 44 noncholinergic for morphology) from 27 mice (56 slices) and 46 BLA-projecting cholinergic neurons from nine macaques (38 slices).

We built two complete data sets. One data set allowed a within-species (mouse) comparison of BLA-projecting NBM/SI neurons, comparing those that were positive for ChAT with those that were not (48 vs. 46, respectively). The other data set provided for a between-species comparison (mouse versus macaque) of

BLA-projecting NBM/SI neurons, all of which were cholinergic. Although there was a considerable diversity both within and between species, our analyses of these two groups revealed important distinctions in both cases. Broadly speaking, mouse BLA-projecting cholinergic neurons are less excitable than mouse BLA-projecting noncholinergic neurons, and macaque BLA-projecting NBM/SI cholinergic neurons are more excitable than mouse BLA-projecting NBM/SI cholinergic neurons. In addition, the soma–proximal arbors of macaque BLA-projecting NBM/SI cholinergic neurons tend to have fewer branch points and occupy larger 3D space than those of mouse.

4.1 | Comparison With Previous Studies

The physiological differences we found between BLA-projecting cholinergic and noncholinergic neurons in the mouse NBM/SI mirrored those of previous studies that examined the basal

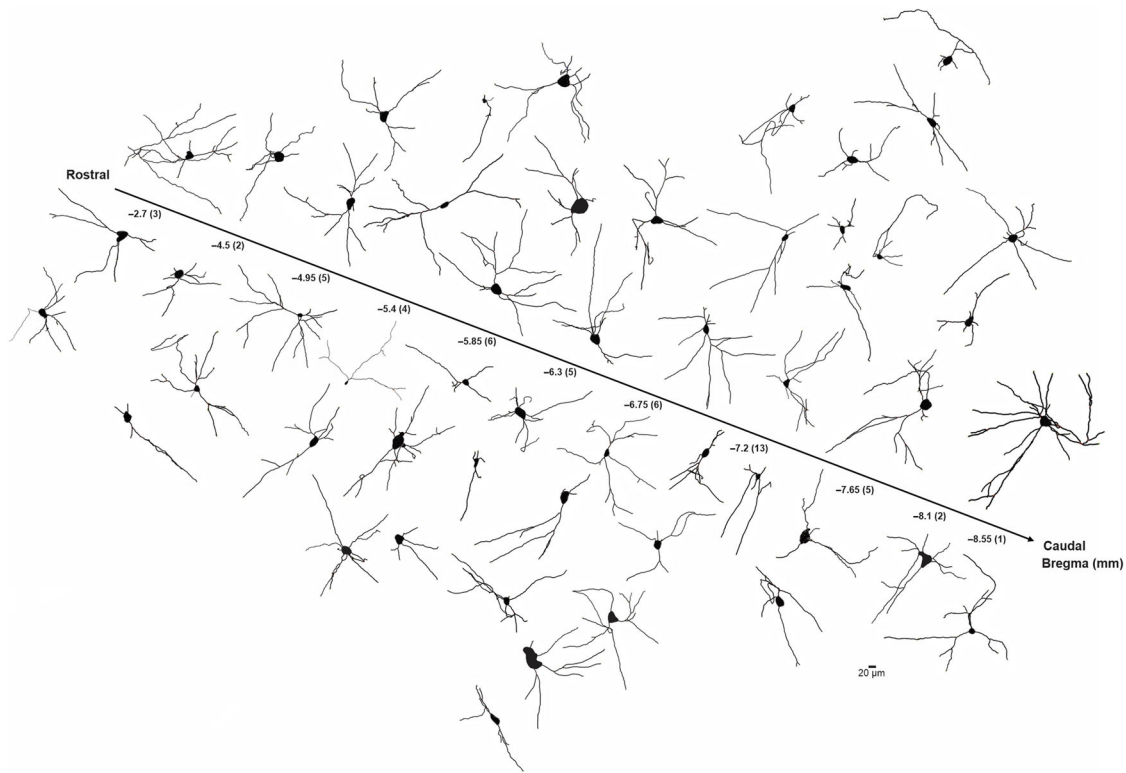


FIGURE 8 | Skeletonized renditions of relocated BLA-projecting cholinergic neurons within NBM/SI along bregma in macaque. The proximal $100^+ \mu\text{m}$ of the processes emanating from cholinergic somata of macaque were morphologically diverse regardless of location along bregma. Most neurons were multipolar, yet fairly simple ($n = 52$).

forebrain using less strict criteria. Those studies were done in guinea pig (Griffith 1988; Alonso et al. 1996), rat (Markram and Segal 1990; Bengtson and Osborne 2000), and mouse (Hedrick and Waters 2010; López-Hernández et al. 2017); in no case did they attempt to identify projection targets. Despite the variety of approaches used to identify and characterize these populations, the most striking and common property of basal forebrain cholinergic neurons is their overall sluggish excitability, with lower spiking rates, more rapid accommodation, and stronger AHP currents, compared with noncholinergic neurons. The overall lower spike frequencies of cholinergic neurons have also been demonstrated using *in vivo* extracellular recordings in mouse (Hangya et al. 2015).

To the best of our knowledge, this is the first study in macaque characterizing basal forebrain cholinergic projection neurons in detail using both patch-clamp physiology and morphometric assays. Prior *in vivo* electrophysiology studies of BFCNs with extracellular recording have shown a mean spontaneous firing rate of 25 Hz in SI neurons from rhesus monkeys (Wilson and Rolls 1990), 20–30 Hz in medial basal forebrain including MS and DB neurons (Ledbetter, Chen, and Monosov 2016), and 40–50 Hz in lateral basal forebrain including VP neurons (Ledbetter, Chen, and Monosov 2016). The firing rate of SI neurons is close to the median value of our macaque cholinergic NBM/SI data set. However, extracellular studies do not assess whether the recorded neurons are cholinergic, potentially complicating these comparisons with our data set.

4.2 | Potential Mechanisms Underlying Observed Physiological Differences

The most obvious source of differences in electrophysiological profiles are variations in the underlying channel-encoding genes, their levels of expression, and/or the cellular distribution of channel proteins. The vast number of channel-encoding genes, their complex regulatory motifs, and their varying contributions to different aspects of excitability preclude narrowing in on a single candidate gene. Nevertheless, it is known that the broad family of K^+ channels (including the various leak, voltage- and calcium-gated K^+ conductances) are important determinants of neuronal excitability, contributing to the latency, duration, and fidelity of spiking with increasing depolarizing steps, as well as to the time course of repolarization and adaptation (Sah and Sah 1996; Betancourt and Colom 2000; Enyedi and Czirjak 2010). A survey of transcriptomic cell types in the mouse nervous system reveals that cholinergic neurons in the pallidum are relatively enriched in their expression of KCNC2 voltage-gated potassium channels in comparison to noncholinergic neurons in the same area (Zeisel et al. 2018), an observation that is at least consistent with our within-species cholinergic versus noncholinergic comparison. Clearly, additional cell-specific transcriptomic experiments are needed to gather in-depth information on the expression patterns of the key conductances in BLA-projecting cholinergic neurons in mouse and macaque. Patch-seq, combining electrophysiological recordings with single-cell transcriptome profiling in the same cells (Lipovsek et al. 2021; Chiou et al. 2023; Yao et al. 2023), would be especially useful.

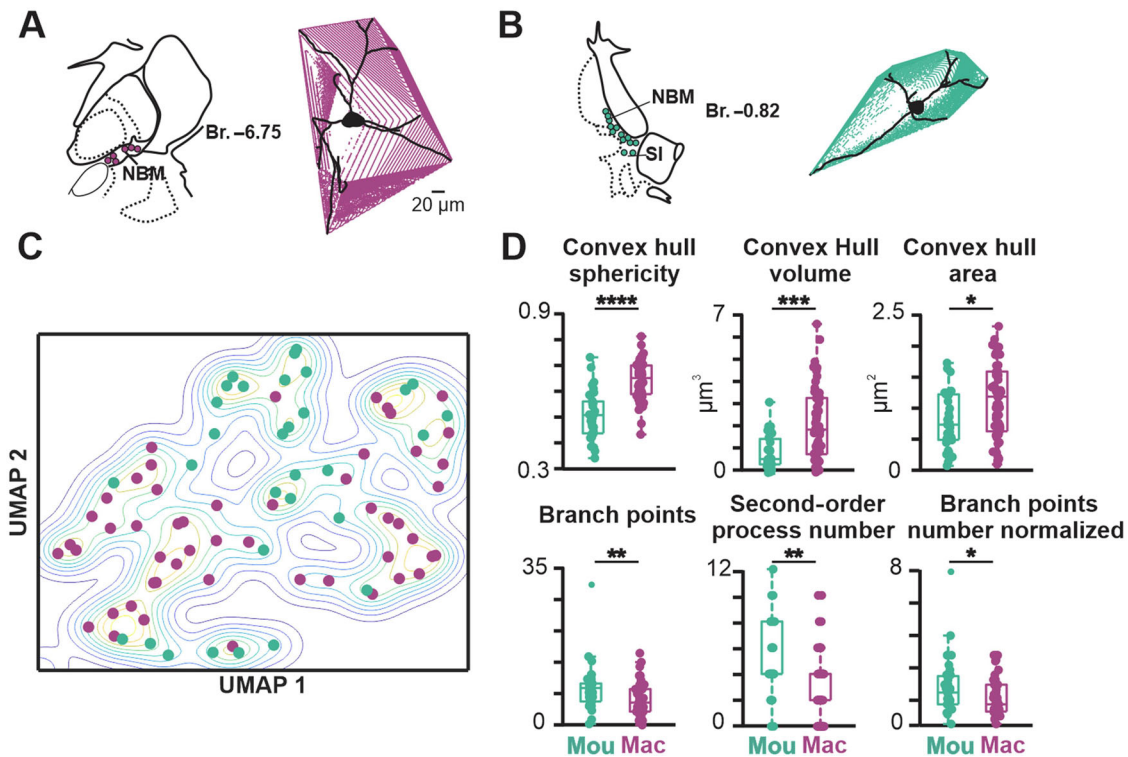


FIGURE 9 | BLA-projecting NBM/SI cholinergic neurons in macaque differ from those in mouse in six of the 13 morphological parameters assessed. See Figures S9-1, S9-2, and S9-3. A. (LHS) Approximate location in hemicoronal diagram of macaque basal forebrain region at approximately -6.75 Bregma. (RHS) A volume rendering of proximal neuritic domain of a representative NBM/SI, BLA-projecting, cholinergic neuron from macaque. B. Approximate location in hemicoronal section of mouse basal forebrain and volume rendering of proximal neurite domain of a representative NBM/SI, BLA-projecting, cholinergic neuron from mouse. C. Nondimensional (UMAP) plot of all 13 morphological features of BLA-projecting NBM/SI cholinergic neurons from macaque (purple, $n = 52$) versus mouse (teal, $n = 31$). Mouse data are from the same set of morphological parameters as presented in Figures 4 and 4-1. D. Population scatter plus box plots of data for the six set of morphological properties that differ between BLA-projecting NBM/SI cholinergic macaque ($n = 52$; purple) compared with mouse ($n = 31$; teal) neurons. Mouse data are from the same set of morphological parameters as presented in Figures 4 and 4-1.

Another possibility is that electrophysiological differences follow from morphological ones. The macaque NBM/SI is much larger in extent than the mouse NBM/SI; compare, for example, the lengths of the rostro-caudal axes in mouse (Figure 3) and macaque (Figure 8). Yet, the differences in the convex hulls of mouse and macaque neurons are much more modest than the relative sizes of their brains might suggest (Figure 9D). Moreover, some of the measured physiological differences are not consistent with size differences. If macaque neurons were simply larger than mouse neurons, everything else kept constant, one would predict that their input resistances would be smaller and their rheobase currents larger. However, in fact, the opposite is true in both cases (Figure 7D). One is forced to look elsewhere, namely to ion channel expression, for an explanation.

4.3 | Physiological Consequences

The physiological differences between mouse and macaque neurons reported here are striking. What makes them remarkable is that in this study we restricted our attention to the BLA-projecting cholinergic neurons of NBM/SI. One might think—and we thought at the outset—that such a well-defined class would have well-defined and conserved properties. Previous studies that compared the intrinsic physiology of similarly well-defined

classes of neurons in mouse and primate (human) neocortex found that physiological properties were indeed largely conserved (Kalmbach et al. 2018, Kalmbach et al. 2021). However, we found that this was not true for this cholinergic neuronal class. Leaving morphology aside, physiology alone cleanly separated mouse from macaque neurons (Figure 7C).

In retrospect, we should not have been surprised because biological systems generally do not require uniformity to produce uniform results. Degeneracy—the idea that biological systems, formed through the complexities of evolution, find multiple solutions to common problems—is an established concept. In neuroscience, it has been made most concrete by work on how different combinations of ion channels produce the same neuronal firing patterns (Prinz, Bucher, and Marder 2004; Haddad and Marder 2018; Seenivasan and Narayanan 2022). Inspired by immunology studies, degeneracy has been suggested as a “first principle” for understanding neural organization generally (Tononi, Sporns, and Edelman 1999; Edelman and Gally 2001).

Individual cholinergic neurons show striking physiological differences. How might they, even so, mediate equivalent behavior? There are multiple possibilities. One set of possibilities is upstream of the NBM/SI. Inhibitory and excitatory inputs

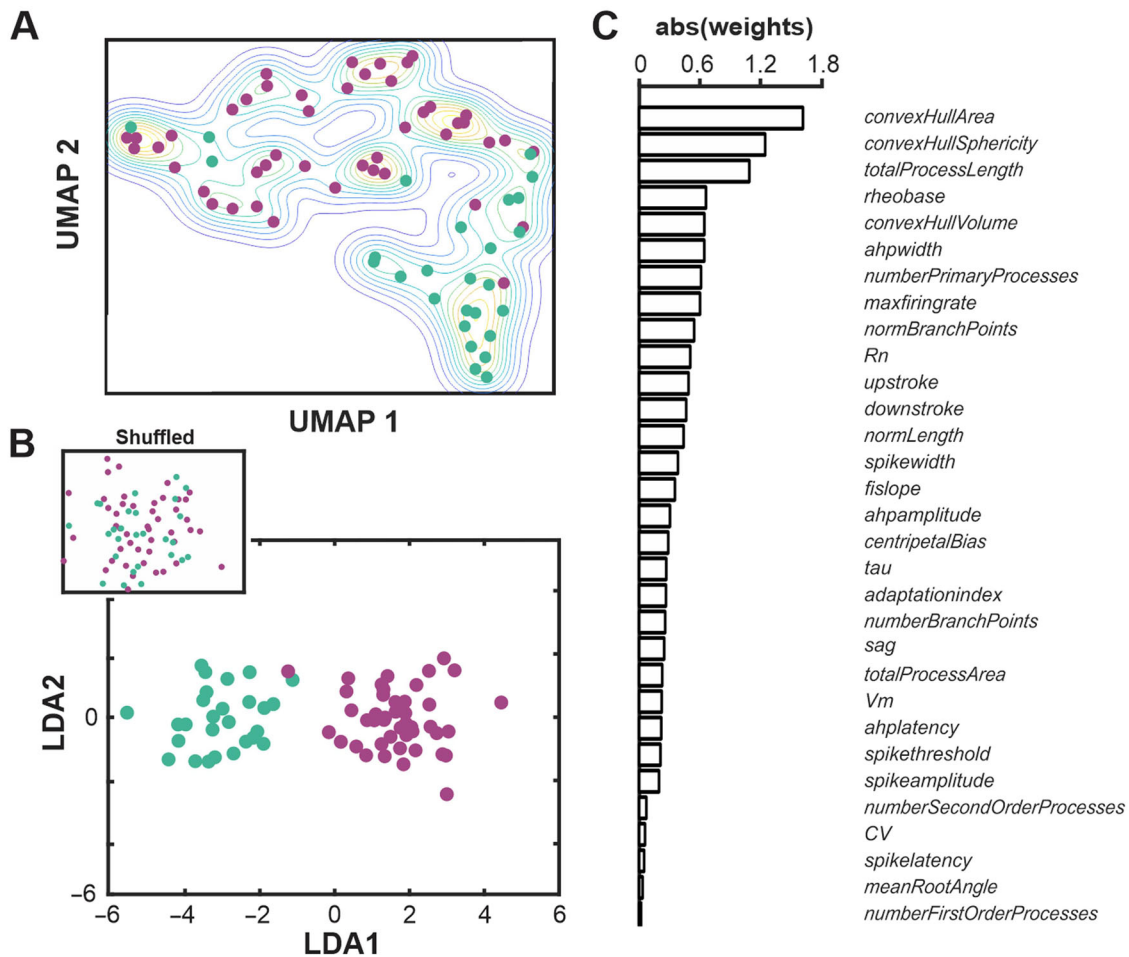


FIGURE 10 | Examination of combined morphoelectric features distinguishes macaque versus mouse basal forebrain neurons despite common projection target, anatomical location, and cholinergic phenotype. **A**. Nondimensional (UMAP) plot of all 18 electrophysiological and 13 morphological features of BLA-projecting NBM/SI cholinergic neurons from macaque (purple, $n = 46$) versus mouse (teal, $n = 27$). **B**. Linear discriminant analysis was applied to all 18 electrophysiological and 13 morphological features of BLA-projecting NBM/SI cholinergic neurons from macaque (purple, $n = 46$) versus mouse (teal, $n = 27$). Note the clear separation in clustering of the two populations from one another and its distinct nature from the distribution of shuffled data (shown in inset). **C**. Plot of the absolute values of the weighted differences for LDA in all 18 electrophysiological and 13 morphological features of BLA-projecting NBM/SI cholinergic neurons from macaque (purple, $n = 46$) versus mouse (teal, $n = 27$).

to the NBM/SI could compensate for the lesser excitability of the mouse neurons if the inhibition they received was sparser or weaker, if the excitation was more distributed or stronger, or if the fluctuations of one or the other were slightly different. A second set of possibilities is downstream of NBM/SI. The cholinergic fibers that NBM/SI neurons send to BLA are notoriously expansive, with long lengths and multiple branch points. Branch point failures, multiple release sites, and pre- and postsynaptic sites of action by acetylcholine in the BLA could potentially contribute (Unal, Pare, and Zaborszky 2015; Jiang et al. 2016). A third set of possibilities has to do with the composition of NBM/SI neurons. Cholinergic neurons represent only a minority of projection neurons in rodents, whereas they represent a majority in primates (Gritti et al. 2006; Zaborszky, van den Pol, and Gyengesi 2012; Mesulam, Mufson, Levey, et al. 1983; Mesulam and Geula 1988; Bañuelos et al. 2023). The interplay between cholinergic and noncholinergic projections is an understudied—and at the moment somewhat mysterious—topic, but it represents a distinct potential mechanism for tuning circuit function.

Although there are many possibilities, most of these are experimentally tractable. One can measure excitatory and inhibitory currents in NBM/SI neurons using patch-clamp recordings, mark PSD95 and gephyrin to count synapses and their distribution (Bensussen et al. 2020), and combine the latest sensors to assess the temporal and spatial profile of acetylcholine release when axons are activated (Sethuramanujam et al. 2021; Zhong et al., unpublished observation). Finally, given that we have built a combined data set of physiological and morphological properties, this is an ideal case for computational methods to provide explanatory power.

Author Contributions

L.W.R. conceived, designed, and supervised the project. F.L. took the lead in coordinating the experiments, making figures, and drafting the manuscript. F.L., L.J., N.S.D., and G.V.W. collected the electrophysiology data. L.B. performed the immunostainings. F.L. collected confocal images, and L.J. reconstructed all cells. N.S.D. wrote the MATLAB

codes and analyzed the data. F.L., L.J., N.S.D., D.A.T., and L.W.R. contribute to figure production, data interpretation, and manuscript revision. M.A.G.E., A.P., and A.M. performed macaque surgery and contributed to the methodology. A.C.C. performed macaque tissue blocking. B.B.A. supplied animals and oversaw the macaque studies. M.A.G.E. and B.B.A. provided comments on an early version of the manuscript. L.W.R. and D.A.T. provided critical feedback and helped shape the project, analysis, and manuscript.

Acknowledgments

This research was supported by NINDS Intramural Research Program (IRP) grants to L.W.R. and D.A.T., and an NIMH IRP grant (ZIA MH002928) to B.B.A. This work was in collaboration with the NIH Comparative Brain Physiology Consortium (formerly Nonhuman Primate Physiology Consortium). The authors thank Dr. G. Fishell and collaborators (Harvard) for the gift of S9E27. This enhancer/virus was included in a subset of the macaque experiments. We also thank Dr. Carolyn Smith for assistance in confocal imaging at the NINDS Light Imaging Core Facility.

Conflicts of Interest

The authors declare no conflicts of interest.

Data Availability Statement

The data that support the findings of this study are openly available in The Dandi Archive at <https://dandiarchive.org/>.

References

Alonso, A., A. Khateb, P. Fort, B. E. Jones, and M. Mühlethaler. 1996. "Differential Oscillatory Properties of Cholinergic and Non-Cholinergic Nucleus Basalis Neurons in Guinea Pig Brain Slice." *European Journal of Neuroscience* 8: 169–182.

Ananth, M. R., P. Rajebhosale, R. Kim, D. A. Talmage, and L. W. Role. 2023. "Basal Forebrain Cholinergic Signalling: Development, Connectivity and Roles in Cognition." *Nature Reviews Neuroscience* 24: 233–251.

Ballinger, E. C., M. Ananth, D. A. Talmage, and L. W. Role. 2016. "Basal Forebrain Cholinergic Circuits and Signaling in Cognition and Cognitive Decline." *Neuron* 91: 1199–1218.

Bañuelos, C., J. R. Kittleson, K. H. LaNasa, et al. 2023. "Cognitive Aging and the Primate Basal Forebrain Revisited: Disproportionate GABAergic Vulnerability Revealed." *Journal of Neuroscience* 43: 8425–8441.

Bengtson, C. P., and P. B. Osborne. 2000. "Electrophysiological Properties of Cholinergic and Noncholinergic Neurons in the Ventral Pallidal Region of the Nucleus Basalis in Rat Brain Slices." *Journal of Neurophysiology* 83: 2649–2660.

Bensussen, S., S. Shankar, K. H. Ching, et al. 2020. "A Viral Toolbox of Genetically Encoded Fluorescent Synaptic Tags." *iScience* 23: 101330.

Betancourt, L., and L. V. Colom. 2000. "Potassium (K⁺) Channel Expression in Basal Forebrain Cholinergic Neurons." *Journal of Neuroscience Research* 61: 646–651.

Bird, A. D., and H. Cuntz. 2019. "Dissecting Sholl Analysis Into Its Functional Components." *Cell Reports* 27: 3081–3096.

Chiou, K. L., X. Huang, M. O. Bohlen, et al. 2023. "A Single-Cell Multi-Omic Atlas Spanning the Adult Rhesus Macaque Brain." *Science Advances* 9: eadh1914.

Crouse, R. B., K. Kim, H. M. Batchelor, et al. 2020. "Acetylcholine Is Released in the Basolateral Amygdala in Response to Predictors of Reward and Enhances the Learning of Cue-Reward Contingency." *eLife* 9: 1–31.

Dal Monte, O., V. D. Costa, P. L. Noble, E. A. Murray, and B. B. Averbeck. 2015. "Amygdala Lesions in Rhesus Macaques Decrease Attention to Threat." *Nature Communications* 6: 10161.

Diehl, M. M., C. Bravo-Rivera, and G. J. Quirk. 2019. "The Study of Active Avoidance: A Platform for Discussion." *Neuroscience and Biobehavioral Reviews* 107: 229–237.

Easton, A., A. E. Fitchett, M. J. Eacott, and M. G. Baxter. 2011. "Medial Septal Cholinergic Neurons Are Necessary for Context-Place Memory but Not Episodic-Like Memory." *Hippocampus* 21: 1021–1027.

Edelman, G. M., and J. A. Gally. 2001. "Degeneracy and Complexity in Biological Systems." *Proceedings National Academy of Science of the United States of America* 98: 13763–13768.

Enyedi, P., and G. Czirjak. 2010. "Molecular Background of Leak K Currents: Two-Pore Domain Potassium Channels." *Physiological Reviews* 90: 559–605.

Fredericks, J. M., K. E. Dash, E. M. Jaskot, et al. 2020. "Methods for Mechanical Delivery of Viral Vectors Into Rhesus Monkey Brain." *Journal of Neuroscience Methods* 339: 108730.

Furlanis, E., M. Dai, B. Leyva Garcia, et al. 2024. *An Enhancer-AAV Toolbox to Target and Manipulate Distinct Interneuron Subtypes*. BioRxiv. <https://doi.org/10.1101/2024.07.17.603924>.

Gore, F., E. C. Schwartz, B. C. Brangers, et al. 2015. "Neural Representations of Unconditioned Stimuli in Basolateral Amygdala Mediate Innate and Learned Responses." *Cell* 162: 134–145.

Griffith, W. H. 1988. "Membrane Properties of Cell Types Within Guinea Pig Basal Forebrain Nuclei in Vitro." *Journal of Neurophysiology* 59: 1590–1612.

Gritti, I., P. Henny, F. Galloni, L. Mainville, M. Mariotti, and B. E. Jones. 2006. "Stereological Estimates of the Basal Forebrain Cell Population in the Rat, Including Neurons Containing Choline Acetyltransferase, Glutamic Acid Decarboxylase or Phosphate-Activated Glutaminase and Colocalizing Vesicular Glutamate Transporters." *Neuroscience* 143: 1051–1064.

Grybko, M. J., E. T. Hahm, W. Perrine, et al. 2011. "A Transgenic Mouse Model Reveals Fast Nicotinic Transmission in Hippocampal Pyramidal Neurons." *European Journal of Neuroscience* 33: 1786–1798.

Haddad, S. A., and E. Marder. 2018. "Circuit Robustness to Temperature Perturbation Is Altered by Neuromodulators." *Neuron* 100: 609–623.

Hangya, B., S. P. Ranade, M. Lorenc, and A. Kepecs. 2015. "Central Cholinergic Neurons Are Rapidly Recruited by Reinforcement Feedback." *Cell* 162: 1155–1168.

Hedrick, T., and J. Waters. 2010. "Physiological Properties of Cholinergic and Non-Cholinergic Magnocellular Neurons in Acute Slices From Adult Mouse Nucleus Basalis." *PLoS ONE* 5: e11046.

Jiang, L., S. Kundu, J. D. Lederman, et al. 2016. "Cholinergic Signaling Controls Conditioned Fear Behaviors and Enhances Plasticity of Cortical-Amygdala Circuits." *Neuron* 90: 1057–1070.

Johansen, J. P., C. K. Cain, L. E. Ostroff, and J. E. Ledoux. 2011. "Molecular Mechanisms of Fear Learning and Memory." *Cell* 147: 509–524.

Kalmbach, B. E., A. Buchin, B. Long, et al. 2018. "h-Channels Contribute to Divergent Intrinsic Membrane Properties of Supragranular Pyramidal Neurons in human Versus Mouse Cerebral Cortex." *Neuron* 100: 1194–1208.

Kalmbach, B. E., R. D. Hodge, N. L. Jorstad, et al. 2021. "Signature Morpho-Electric, Transcriptomic, and Dendritic Properties of Human Layer 5 Neocortical Pyramidal Neurons." *Neuron* 109: 2914–2927.

Knox, D., and S. M. Keller. 2016. "Cholinergic Neuronal Lesions in the Medial Septum and Vertical Limb of the Diagonal Bands of Broca Induce Contextual Fear Memory Generalization and Impair Acquisition of Fear Extinction." *Hippocampus* 26: 718–726.

Ledbetter, N. M., C. D. Chen, and I. E. Monosov. 2016. "Multiple Mechanisms for Processing Reward Uncertainty in the Primate Basal Forebrain." *Journal of Neuroscience* 36: 7852–7864.

LeDoux, J. 2012. "Rethinking the Emotional Brain." *Neuron* 73: 653–676.

- LeDoux, J. E. 2022. "As Soon as There Was Life, There Was Danger: The Deep History of Survival Behaviours and the Shallower History of Consciousness." *Philosophical Transactions of the Royal Society B: Biological Sciences* 377: 20210292.
- Lipovsek, M., C. Bardy, S. J. Tripathy, C. R. Cadwell, K. Hadley, and D. Kobak. 2021. "Patch-seq: Past, Present, and Future." *Journal of Neuroscience* 41: 937–946.
- López-Hernández, G. Y., M. Ananth, L. Jiang, E. C. Ballinger, D. A. Talmage, and L. W. Role. 2017. "Electrophysiological Properties of Basal Forebrain Cholinergic Neurons Identified by Genetic and Optogenetic Tagging." *Journal of Neurochemistry* 142: 103–110.
- Markram, H., and M. Segal. 1990. "Electrophysiological Characteristics of Cholinergic and Non-Cholinergic Neurons in the Rat Medial Septum-Diagonal Band Complex." *Brain Research* 513: 171–174.
- McGaugh, J. L. 2018. "Emotional Arousal Regulation of Memory Consolidation." *Current Opinion in Behavioral Sciences* 19: 55–60.
- McInnes, L., J. Healy, N. Saul, and L. Großberger. 2018. "UMAP: Uniform Manifold Approximation and Projection." *The Journal of Open Source Software* 3: 861.
- Melamed, J. L., F. M. de Jesus, R. S. Maior, and M. Barros. 2017. "Scopolamine Induces Deficits in Spontaneous Object-Location Recognition and Fear-Learning in Marmoset Monkeys." *Frontiers in Pharmacology* 8: 1–10.
- Mesulam, M. M., and C. Geula. 1988. "Nucleus Basalis (Ch4) and Cortical Cholinergic Innervation in the Human Brain: Observations Based on the Distribution of Acetylcholinesterase and Choline Acetyltransferase." *Journal of Comparative Neurology* 275: 216–240.
- Mesulam, M. M., E. J. Mufson, A. I. Levey, and B. H. Wainer. 1983. "Cholinergic Innervation of Cortex by the Basal Forebrain: Cytochemistry and Cortical Connections of the Septal Area, Diagonal Band Nuclei, Nucleus Basalis (Substantia Innominata), and Hypothalamus in the Rhesus Monkey." *Journal of Comparative Neurology* 214: 170–197.
- Mesulam, M. M., E. J. Mufson, B. H. Wainer, and A. I. Levey. 1983. "Central Cholinergic Pathways in the Rat: An Overview Based on an Alternative Nomenclature (Ch1-Ch6)." *Neuroscience* 10: 1185–1201.
- Murray, E. A., and L. K. Fellows. 2022. "Prefrontal Cortex Interactions With the Amygdala in Primates." *Neuropsychopharmacology* 47: 163–179.
- Picciotto, M. R., M. J. Higley, and Y. S. Mineur. 2012. "Acetylcholine as a Neuromodulator: Cholinergic Signaling Shapes Nervous System Function and Behavior." *Neuron* 76: 116–129.
- Prinz, A. A., D. Bucher, and E. Marder. 2004. "Similar Network Activity From Disparate Circuit Parameters." *Nature Neuroscience* 7: 1345–1352.
- Rajebhosale, P., M. R. Ananth, R. Kim, et al. 2024. "Functionally Refined Encoding of Threat Memory by Distinct Populations of Basal Forebrain Cholinergic Projection Neurons." *eLife* 13: e86581.
- Ridley, R. M., P. Pugh, C. J. MacLean, and H. F. Baker. 1999. "Severe Learning Impairment Caused by Combined Immunotoxic Lesion of the Cholinergic Projections to the Cortex and Hippocampus in Monkeys." *Brain Research* 836: 120–138.
- Sah, P., and P. Sah. 1996. "Ca²⁺-Activated K⁺ Currents in Neurons: Types, Physiological Roles and Modulation." *Trends in Neuroscience* 19: 150–154.
- Sah, P., Y. Sun, and H. Gooch. 2020. "Fear Conditioning and the Basolateral Amygdala." *FI000Research* 9: 1–8.
- Saunders, R. C., T. G. Aigner, and J. A. Frank. 1990. "Magnetic Resonance Imaging of the Rhesus Monkey Brain: Use for Stereotactic Neurosurgery." *Experimental Brain Research* 81: 443–446.
- Seenivasan, P., and R. Narayanan. 2022. "Efficient Information Coding and Degeneracy in the Nervous System." *Current Opinion in Neurobiology* 76: 102620.
- Semba, K. 2004. "Phylogenetic and Ontogenetic Aspects of the Basal Forebrain Cholinergic Neurons and Their Innervation of the Cerebral Cortex." *Progress in Brain Research* 145: 1–43.
- Sethuramanujam, S., A. Matsumoto, G. deRosenroll, et al. 2021. "Rapid Multi-Directed Cholinergic Transmission in the Central Nervous System." *Nature Communications* 12: 1374.
- Ting, J. T., B. R. Lee, P. Chong, et al. 2018. "Preparation of Acute Brain Slices Using an Optimized N-Methyl-D-glucamine Protective Recovery Method." *Journal of Visualized Experiments* 2018: 1–13.
- Tononi, G., O. Sporns, and G. M. Edelman. 1999. "Measures of Degeneracy and Redundancy in Biological Networks." *Proceedings of the National Academy of Sciences of the United States of America* 96: 3257–3262.
- Turchi, J., R. C. Saunders, and M. Mishkin. 2005. "Effects of Cholinergic Deafferentation of the Rhinal Cortex on Visual Recognition Memory in Monkeys." *Proceedings of the National Academy of Sciences of the United States of America* 102: 2158–2161.
- Tye, K. M. 2018. "Neural Circuit Motifs in Valence Processing." *Neuron* 100: 436–452.
- Unal, C. T., D. Pare, and L. Zaborszky. 2015. "Impact of Basal Forebrain Cholinergic Inputs on Basolateral Amygdala Neurons." *Journal of Neuroscience* 35: 853–863.
- Walbridge, S., G. J. A. Murad, J. D. Heiss, E. H. Oldfield, and R. R. Lonser. 2006. "Technique for Enhanced Accuracy and Reliability in Non-Human Primate Stereotaxy." *Journal of Neuroscience Methods* 156: 310–313.
- Wilson, F. A. W., and E. T. Rolls. 1990. "Neuronal Responses Related to Reinforcement in the Primate Basal Forebrain." *Brain Research* 509: 213–231.
- Woolf, N. J. 1991. "Cholinergic Systems in Mammalian Brain and Spinal Cord." *Progress in Neurobiology* 37: 475–524.
- Yao, Z., C. T. van Velthoven, M. Kunst, et al. 2023. "A High-Resolution Transcriptomic and Spatial Atlas of Cell Types in the Whole Mouse Brain." *Nature* 624: 317–332.
- Zaborszky, L., A. N. van den Pol, and E. Gyengesi. 2012. "The Basal Forebrain Cholinergic Projection System in Mice." In *The Mouse Nervous System*, edited by C. Watson, G. Paxinos, and L. Puelles, 684–718. Cambridge, MA: Academic Press.
- Zeisel, A., H. Hochgerner, P. Lönnerberg, et al. 2018. "Molecular Architecture of the Mouse Nervous System." *Cell* 174: 999–1014.

Supporting Information

Additional supporting information can be found online in the Supporting Information section.